Simulating Cosmic Reionisation
Pawlik, A.H.

Citation
Pawlik, A. H. (2009, September 30). *Simulating Cosmic Reionisation*. Retrieved from https://hdl.handle.net/1887/14025

Version:	Corrected Publisher's Version
License:	
Downloaded from:	

Note: To cite this publication please use the final published version (if applicable).

CHAPTER 6

Radiative transfer simulations of cosmic reionisation

Andreas H. Pawlik & Joop Schaye

In preparation.

R ADIATIVE transfer (RT) simulations coupled to cosmological hydrody-
namical simulations are one of the most promising tools to study reion-
isation, a key epoch in the high-redshift Universe. Current generations
of RT schemes are, however, often limited for use with uniform and rela-
tively coarse grids that imply a spatial resolution far below that of state-of-
the-art spatially adaptive hydrodynamical simulations. Small-scale struc-
ture in the cosmic gas is then, at best, only statistically accounted for. Here
we use the spatially adaptive RT scheme TRAPHIC (Chapter 4) to investigate
the implications of this approximate approach. We contrast RT simulations
performed on spatially adaptive smoothed particle hydrodynamics density
fields with RT simulations performed on density fields that are defined on a
uniform grid. Comparisons of the evolution of the mean ionised fraction, of
the dependence of the ionised fraction on the local gas density and of power
spectra of the 21 cm signal from neutral hydrogen reveal substantial differ-
ences caused by the difference in the dynamic range employed by the two
types of RT simulations. Our results underpin earlier suggestions that ig-
noring the inhomogeneous distribution of gas on small scales, as is typically
done in current RT simulations of reionisation, can give rise to misleading
conclusions about the spatial distribution of the ionised gas and hence af-
fect the interpretation of current and the predictions of future observations
of reionisation.

6.1 INTRODUCTION

The first stars and galaxies are thought to have formed a few hundred million years after the Big Bang, when the Universe had only a small fraction of its present age. Their radiation transformed the previously cold and neutral hydrogen that filled intergalactic space into the hot and ionised plasma that is observed today. This milestone in the history of the Universe is called the epoch of reionisation (e.g., Barkana & Loeb 2001; Ciardi & Ferrara 2005; Loeb, Ferrara, & Ellis 2008; Choudhury 2009).

Much about reionisation is still unknown. When did reionisation occur? Was it a (nearly) instantaneous event or a complex process of extended duration? How did it proceed? What were the properties of the stars and galaxies that reionised the Universe? Theoretical studies of the epoch of reionisation are currently particularly timely because of the wealth of observational data of unparallelled quality that will soon be provided by a new generation of observatories.

Radio interferometers like LOFAR[1], MWA[2] and SKA[3] will open a previously unexplored observational window by surveying the Universe at very low frequencies with unprecedented high resolution and sensitivity. By mapping the redshifted 21 cm signal from the neutral hydrogen, these interferometers will provide a three-dimensional tomographic view on the intergalactic gas in the distant Universe and offer one of the most direct probes of its evolution during reionisation to date. The infrared space-based observatory JWST[4] and the optical ground-based adaptive optics telescope ELT[5] will even enable the direct imaging of the sources responsible for the reionisation process.

If the Universe was indeed reionised by the first stars, then the high-density gas in and around the halos in which these stars formed must have been ionised first (e.g., Barkana & Loeb 2001). Consequently, reionisation started from the inside out. The low-density gas far away from the first sites of star formation would only be reionised once the ionising radiation was channelled into the large-scale voids (Ciardi, Stoehr, & White 2003). Towards the end, reionisation would, on the other hand, proceed from the outside in (Miralda-Escudé, Haehnelt, & Rees 2000), with the ionising radiation slowly carving its way from the highly ionised voids into the remaining dense pockets of neutral gas.

The depicted scenario is supported by the results of early radiative transfer (RT) simulations (e.g., Sokasian et al. 2003; Gnedin 2000; Nakamoto, Umemura, & Susa 2001) and detections of Lyman-limit systems in the observed spectra of distant ($z \lesssim 6$) quasars (e.g., Fan, Carilli, & Keating 2006). It gave rise to the construction of semi-analytic models of reionisation targeted to investigate the epoch of reionisation in either of the two limiting topological regimes (e.g., Miralda-Escudé, Haehnelt, & Rees 2000; Furlanetto, Zaldarriaga, & Hernquist 2004). More recent RT simulations and semi-analytical models draw a more complex picture. While some works (e.g., Lee et al. 2008) confirm the traditional view of reionisation proceeding inside-out with a reversal to outside-in, others (e.g. Iliev et al. 2006; McQuinn et al. 2007; Zahn et al. 2007) predict that reionisation occurs in a strictly inside-out manner.

The different conclusions may be the result of the fact that many of even the most advanced reionisation simulations lack adequate spatial resolution. To keep the computations feasible, many state-of-the-art RT schemes require the use of uniform grids with relatively few grid points. Combined with the fact that large simulation boxes are necessary to model representa-

---

[1]http://www.lofar.org
[2]http://www.haystack.mit.edu/ast/arrays/mwa/
[3]http://www.skatelescope.org
[4]http://www.jwst.nasa.gov/
[5]http://www.eso.org/sci/facilities/eelt/

tive volumes of the Universe (Barkana & Loeb 2004; Iliev et al. 2006), this means that the spatial resolution of state-of-the-art RT simulations is typically far below that of routine hydrodynamical simulations of galaxy formation. Small-scale clumpiness of the cosmic gas is therefore, if at all, only statistically accounted for. Many RT simulations ignore hydrodynamical effects altogether and assume the gas to trace the dark matter.

Some works (e.g., Furlanetto & Oh 2005; Choudhury, Haehnelt, & Regan 2009; Finlator, Özel, & Davé 2009) have argued that a proper modelling of the inhomogeneous distribution of gas on small scales could, however, play a critical role in determining the topology of the ionised gas, because it strongly affects the computation of recombination rates (e.g., Gnedin & Ostriker 1997; Miralda-Escudé, Haehnelt, & Rees 2000; Kohler, Gnedin, & Hamilton 2007; Pawlik, Schaye, & van Scherpenzeel 2009a). In fact, Choudhury, Haehnelt, & Regan (2009) showed that due to the inhomogeneous nature of recombinations, the ionised fraction shows a non-trivial dependence on the local gas density.

Here we present preliminary results from an ongoing project to study the progress, topology and observability of reionisation using accurate, spatially adaptive RT simulations in combination with high-resolution hydrodynamical simulations of the high-redshift Universe. We will employ our RT scheme TRAPHIC (Chapter 4) on top of cosmological hydrodynamical simulations performed with the N-body/Tree-PM/SPH code P-GADGET3-BG, an enhanced version of GADGET-2 (Springel 2005), to follow the propagation of ionising photons emitted by the first galaxies and to compute their interaction with the cosmic gas. TRAPHIC has been specifically designed for use with large, spatially adaptive simulations of reionisation and hence is well-suited for the current project. Its distinguishing properties that enable these types of simulations are that it is spatially adaptive, that its computation time does not directly scale with the number of radiation sources and that it operates in parallel on distributed memory machines.

We will use TRAPHIC to carry out spatially adaptive RT simulations of reionisation by post-processing static density fields provided by the spatially adaptive SPH simulation we perform. Although the current version of TRAPHIC can also be employed to perform RT simulations in step with the hydrodynamical evolution, we have chosen the commonly employed post-processing technique and the static approximation to facilitate a comparison with previous works. The RT simulations are performed directly on top of the SPH particle distribution and hence fully exploit the available dynamic range. We will also carry out RT simulations on top of density fields obtained by first mapping the SPH particles onto a uniform grid and then Monte-Carlo sampling it for use with TRAPHIC. These simulations hence do not employ the full dynamic range exhibited by the SPH simulation. The analysis of the results obtained in these two types of RT simulations and their comparison will allow us to judge the importance of performing RT simulations that exploit the full dynamic range inherent to the underlying hydrodynamical simulation.

This chapter is organised as follows. We describe our SPH simulation method and explain our approach to accomplish the transport of ionising radiation in Sec. 6.2. We present our results in Sec. 6.3, where we employ various statistics to discuss the differences between the spatially adaptive RT simulations performed on density fields obtained directly from the SPH simulation and the RT simulations that are performed on density fields obtained by interpolating the densities from the SPH simulation to a uniform grid. We summarise our conclusions and discuss the limitations of the present work in Sec. 6.4. Throughout we assume a flat ΛCDM universe and employ the set of cosmological parameters $\Omega_{\mathrm{m}} = 0.258$, $\Omega_{\mathrm{b}} = 0.0441$, $\Omega_{\Lambda} = 0.742$, $\sigma_8 = 0.796$, $n_{\mathrm{s}} = 0.963$, $h = 0.719$, in agreement with the WMAP 5-year observations (Komatsu et al. 2008).

6.2 SIMULATIONS

In this section we describe the RT simulations that we employ for the present study. The RT is carried out by post-processing static SPH density fields obtained from a cosmological hydrodynamical simulation. The hydrodynamical simulation is performed using a modified version of the SPH code GADGET-2 (Springel 2005). We describe it in Sec. 6.2.1. The RT simulations make use of the spatially adaptive RT scheme TRAPHIC (Chapter 4) and are described in Sec. 6.2.2.

We perform the RT both on top of the density fields obtained directly from the spatially adaptive hydrodynamical simulation and on top of density fields generated by mapping the SPH particles from the hydrodynamical simulation to a uniform grid. We briefly illustrate the difference in dynamic range exhibited by the two types of density fields used in the RT simulations in Sec. 6.2.3.

6.2.1 Cosmological N-body/SPH simulations

We use P-GADGET3-BG, a modified version of the SPH code GADGET-2 (Springel 2005). The initial dark matter (DM) and SPH particle positions and velocities are obtained from glass-like initial conditions using CMBFAST (version 4.1; Seljak & Zaldarriaga 1996) and employing the Zeldovich approximation to evolve the particles down to the initial simulation redshift $z = 127$.

The gas is of primordial composition, with a hydrogen mass fraction $X = 0.752$ and a helium mass fraction $Y = 1 - X$. It is allowed to cool by collisional ionisation and excitation, emission of free-free and recombination radiation and Compton cooling off the cosmic microwave background. Molecular hydrogen is kept photo-dissociated at all times by the inclusion of a soft UV background. The implementation of the cooling is described in Wiersma, Schaye, & Smith (2009).

We employ the star formation recipe of Schaye & Dalla Vecchia (2008) to convert SPH particles into star particles. Briefly, gas with densities exceeding the critical density for the onset of the thermo-gravitational instability (hydrogen number densities $n_H = 10^{-2} - 10^{-1}$ cm^{-3}) is expected to be multiphase and star-forming (Schaye 2004). We therefore impose an effective equation of state (EoS) with pressure $P \propto \rho^{\gamma_{\rm eff}}$ for densities $n_H > n_H^*$, where $n_H^* \equiv 10^{-1}$ cm^{-3}, normalised to $P/k = 10^3$ cm^{-3} K at the critical density n_H^*. We use $\gamma_{\rm eff} = 4/3$ for which both the Jeans mass and the ratio of the Jeans length and the SPH kernel are independent of the density, thus preventing spurious fragmentation due to a lack of numerical resolution. Gas on the effective EoS is allowed to form stars using a pressure-dependent rate that reproduces the observed Kennicutt-Schmidt law (Kennicutt 1998), renormalised by a factor of $1/1.65$ to account for the fact that it assumes a Salpeter IMF whereas we are using a Chabrier IMF (Chapter 2).

We perform a single simulation, using $N_{\rm DM} = 64^3$ equal-mass DM particles and $N_{\rm SPH} = 64^3$ equal-mass SPH particles in a box of comoving size $L_{\rm box} = 1.5625 \ h^{-1}$ Mpc. The number of SPH particles decreases during the simulation as SPH particles are transformed into star particles. The gravitational forces are softened over a length of $1/25$ of the mean DM interparticle distance, and we employ $N_{\rm ngb} = 48$ SPH neighbours for computing the SPH properties of the SPH particles. Our choice for the particle number and the box size results in DM and SPH particle masses of $8.3 \times 10^5 \ h^{-1}$ M$_\odot$ and $1.8 \times 10^5 \ h^{-1}$ M$_\odot$, respectively, and hence a relatively high mass resolution: atomic coolers, i.e. halos with virial temperature $T_{\rm vir} \sim 10^4$ K, corresponding to masses $M_{\rm DM} \sim 10^8 \ h^{-1}$ M$_\odot$, which in the absence of molecular hydrogen and metal line cooling constitute the first sites of star formation (for a review see, e.g., Barkana & Loeb 2001), are resolved with more than 100 particles. Note that our choice for box size and

mass resolution implies a spatial resolution that is high compared with that encountered in typical cosmological RT simulations.

The simulation box employed in the present study is, however, comparatively small. Representative models of the Universe during reionisation require simulation boxes of at least $30\ h^{-1}$ Mpc (Barkana & Loeb 2004; Iliev et al. 2006). Simulating the field of view of future epoch-of-reionisation observatories (see Sec. 6.3.3) will require even larger simulation boxes (e.g., Mellema et al. 2006). Our choice for the simulation box is a direct consequence of our choice for the particle number, which we wish to keep low to allow for a quick exploration of the parameter space in this *pilot* study. Simulations that employ the same particle number but use a significantly larger box would lack the resolution to form (a sufficient number of) star particles required for the RT simulations performed here. We note that for the present choice of box size and particle number, the number of star particles formed until redshift 6.0 (8.8) is 815 (49), which is still very low.

Simulation snapshots are generated at 100 equally spaced redshifts between $z = 20$ and $z = 6$. The SPH densities from these snapshots are processed to generate gas density fields on a uniform grid with $N_{\mathrm{g}} = 64^3$ points using mass-conserving SPH interpolation (e.g., Alvarez, Bromm, & Shapiro 2006). We will perform RT simulations on top of both the original, spatially adaptive and the uniformly gridded SPH density fields. Note that, as a result of the relatively small simulation box, the physical (proper) size of individual grid cells is only $\approx 2\ h^{-1}$ kpc $((1+z)/10)^{-1}$ and hence small compared to the sizes of grid cells employed in typical cosmological RT simulations. The spatial resolution employed in the RT simulations that are performed on the uniformly gridded density fields is therefore still comparatively high, which will likely lead us to strongly underestimate the importance of performing spatially adaptive RT simulations to study reionisation.

6.2.2 Radiative transfer

The RT simulations employ the RT scheme TRAPHIC presented in Chapter 4. Before describing the set-ups of the simulations, we briefly recall the main characteristics of TRAPHIC and explain the parameters that control its performance.

TRAPHIC is a RT scheme for use with SPH simulations that solves the RT equation in a spatially adaptive manner by tracing photons from radiation sources directly on the unstructured grid comprised by the SPH particles. Hence, it is ideally suited for the present study which aims to investigate the difference between RT simulations of reionisation that exploit the full dynamic range of the underlying cosmological hydrodynamical simulation and those that do not. Photons are traced by propagating photon packets from particles to their $\tilde{N}_{\mathrm{ngb}}$ neighbours inside cones. The introduction of cones is necessary to accomplish the transport of radiation in a directed manner on the generally highly irregular distribution of the SPH particles. The opening angle Ω of the cones determines the formal angular resolution of the RT. It is conveniently expressed in terms of a cone number, $N_{\mathrm{c}} \equiv 4\pi/\Omega$.

The photon transport proceeds in two parts. First, source particles emit photon packets to their $\tilde{N}_{\mathrm{ngb}}$ neighbouring SPH particles by means of a set of N_{c} tessellating emission cones. The number of neighbours $\tilde{N}_{\mathrm{ngb}}$ is a parameter that is usually matched to the number of neighbours N_{ngb}, residing in a sphere of radius h (the SPH *kernel*), that is used in the computation of the particle's SPH properties, $\tilde{N}_{\mathrm{ngb}} \lesssim N_{\mathrm{ngb}}$. The use of a fixed number of neighbours $\tilde{N}_{\mathrm{ngb}}$ renders the RT spatially adaptive, and the choice $\tilde{N}_{\mathrm{ngb}} \lesssim N_{\mathrm{ngb}}$ exploits the full dynamic range inherent to the underlying hydrodynamical simulation. Second, the photon packets received

by the neighbouring SPH particles are propagated further downstream. They are confined to the emission cones into which they were originally emitted through the use of transmission cones of solid angle $4\pi/N_c$. The transport is performed using RT time steps of size Δt_r. After each such time step, the properties of the SPH particles are updated according to their interactions (absorptions, scatterings) with the photon packets. We refer the reader to Chapter 4 for a more detailed description of TRAPHIC.

The RT simulations are performed by post-processing the (static) density fields obtained from the cosmological SPH simulation described above. We mention that TRAPHIC can already be employed for RT simulations performed in step[6] with the hydrodynamical evolution of the gas in simulations with P-GADGET3-BG. We opted for the post-processing approach because it enables a more direct comparison between the results obtained in RT simulations performed on top of the original SPH density fields and those performed on top of the associated uniformly gridded density fields. The RT simulations start at redshift $z = 8.94$ (with the formation of the first stars), using the density fields at redshifts $z_i = 8.94 - 0.14i$, where $i = 1, ..20$. For each density field, the RT simulations are performed over the redshift interval $\Delta z = 0.14$, corresponding to the time between two consecutive snapshots.

We assume that all star particles that were formed up to the redshift of the current density field are ionising sources, each of which emits 10^{51} ionising photons per second. The ionising luminosities were roughly chosen such as to achieve reionisation in the simulations that are performed on top of the SPH density fields from the hydrodynamical simulation by the final simulation redshift $z = 6$. We verified that with the employed luminosities, the reionisation histories in our simulations are in (1-sigma) agreement with current constraints on the electron scattering optical depth (Komatsu et al. 2008). We have adopted this simplified approach to facilitate the comparison between the different simulations we perform. We note that we have already coupled TRAPHIC to the population synthesis models of Bruzual & Charlot (2003) that allow the determination of ionising luminosities as a function of the stellar mass, the age and the metalicity of star particles. We will employ this feature in future work in order to consider more realistic source populations.

We refer to the RT simulation that is performed directly on top of the snapshots from the hydrodynamical simulation as *rt-sph*. This simulation fully exploits the available dynamic range of the underlying hydrodynamical simulation. The simulation that is performed using SPH particle positions obtained by Monte-Carlo sampling the associated uniformly gridded density fields is referred to as *rt-grid*. The Monte Carlo sampling is performed by replacing every grid cell i by $N_{SPH}^i = M_i/m$ SPH particles (randomly distributed within the volume of the grid cell) of equal mass, where M_i is the mass of the cell and m is the SPH particle mass. If N_{SPH}^i is not an integer, we draw a random number from a uniform distribution on the interval (0,1) and place an additional particle if this number is smaller than the difference between N_{SPH}^i and the nearest lower integer. We target a total of $N_{SPH} = 64^3$ SPH particles (i.e. the same number of particles as for the original SPH simulation). Since the Monte Carlo sampling only results in the approximate equality $\sum_i N_{SPH}^i \approx N_{SPH}$, we adjust the particle masses a posteriori to conserve mass, i.e. $m \rightarrow m \times N_{SPH}/\sum_i N_{SPH}^i$. After the particles have been placed, we calculate their densities using the SPH formalism of P-GADGET3-BG, with $N_{ngb} = 48$.

In this work we solve the time-independent RT equation. We will contrast our results to results obtained from solving the time-dependent RT equation in future work. We use a fixed RT time step $\Delta t_r = 10^{-1}$ Myr, during which photons are propagated over a single inter-particle

---

[6]The current implementation still ignores, however, the radiation-hydrodynamical feedback. The radiation-hydrodynamical coupling of TRAPHIC will be presented in a future work.
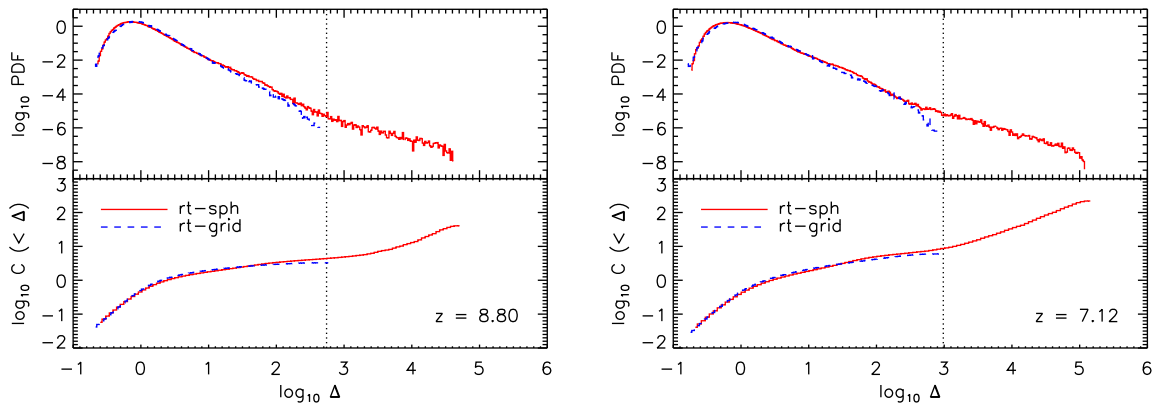
Figure 6.1: *Top panels:* volume-weighted PDF of the gas overdensity Δ per unit $\log_{10} \Delta$ for simulations *rt-sph* (solid red histogram) and *rt-grid* (blue dashed histogram) at redshifts $z = 8.80$ (left) and $z = 7.12$ (right). *Bottom panels:* volume-weighted clumping factor $C(< \Delta)$ of gas with overdensity $< \Delta$ corresponding to the PDFs shown in the top panel. The vertical dotted lines indicate the (redshift-dependent) overdensity corresponding to the (physical) star formation threshold hydrogen density $n_H^* \equiv 10^{-1}$ cm^{-3} (Sec. 6.2.1). Note that the dynamic range exhibited by the spatially adaptive *rt-sph* simulation is more than two orders of magnitude larger than the dynamic range exhibited by the *rt-grid* simulation.

distance only, as explained in Sec. 5.3.3 of Chapter 5. We demonstrate in App. 6.A that the RT time step is sufficiently small to obtain converged results. We furthermore use an angular resolution of $N_c = 32$, which we show to be sufficiently high to obtain converged results in App. 6.A, and set $\tilde{N}_{\mathrm{ngb}} = 32$. We do not employ the density field resampling technique introduced in Chapter 5.

In performing the RT we assume that the gas consists purely of hydrogen, i.e. we set $X = 1$, despite that fact that the SPH simulation employed primordial abundances. This is because we have not yet implemented helium in TRAPHIC. Photons are transported using a single frequency bin in the grey approximation (Sec. 5.3.5 in Chapter 5). We employ a grey photo-ionisation cross-section $\sigma_{\mathrm{HI}} = 6.3 \times 10^{-18}$ cm^2, corresponding to a black-body spectrum of temperature $T = 10^5$ K for the ionising sources (Chapter 7). We assume a constant temperature of $T = 10^4$ K for the ionised gas and compute recombinations in the case B approximation, using a recombination coefficient $\alpha_B = 2.59 \times 10^{-13}$ cm^3 s^{-1} (appropriate for the assumed gas temperature). The ionised fraction of the SPH particles is initially set to zero and is appropriately transferred between the density fields during each simulation. The boundaries of the simulation box are transmissive, i.e. photons leaving the box are lost from the computational domain.

6.2.3   Density field comparison

Before we present our results, we briefly illustrate the difference in the dynamic ranges between the *rt-sph* and the *rt-grid* simulation (Fig. 6.1).

The top panels in Fig. 6.1 show the redshift $z = 8.80$ (left) and the redshift $z = 7.12$ (right) volume-weighted probability density function (PDF) of the gas overdensity $\Delta \equiv \rho/\langle\rho\rangle$, where ρ is the SPH particle gas density and $\langle\rho\rangle$ is the cosmic average gas density. The minimum particle overdensity present is similar in both simulations, but the *rt-sph* simulation contains

particles with overdensities more than two orders of magnitude larger than the largest particle overdensities in the *rt-grid* simulation.

The bottom panels of Fig. 6.1 show the volume-weighted gas clumping factor

$$C(< \Delta) \equiv \langle \rho^2 \rangle_{<\Delta} / \langle \rho \rangle^2, \tag{6.1}$$

where the brackets $\langle \rangle_{<\Delta}$ indicate an average over all gas particles with overdensities $< \Delta$. The (overdensity-dependent) clumping factor $C(< \Delta)$ is a convenient measure for the average recombination rate of gas with overdensities $< \Delta$ (Miralda-Escudé, Haehnelt, & Rees 2000). We computed it by performing a volume-weighted summation over all SPH particles with overdensities $< \Delta$ (cp. Chapter 2),

$$C(< \Delta) = \frac{\sum_{\Delta_i < \Delta} V_i \Delta_i^2}{\sum_{\Delta_i < \Delta} V_i}, \tag{6.2}$$

where $V_i \equiv h_i^3$ is the characteristic volume of SPH particle i, h_i is the radius of its SPH smoothing kernel and Δ_i is its gas overdensity.

For overdensities $\log_{10} \Delta \lesssim 2$ the clumping factors obtained from the two simulations largely agree. For overdensities $\log_{10} \Delta \gtrsim 2$ the clumping factor obtained from the simulation *rt-sph* is, however, significantly larger than that obtained from the simulation *rt-grid*. Averaged over all SPH particles, the clumping factor obtained from *rt-sph* is more than an order of magnitude larger than the clumping factor obtained from *rt-grid*. We may therefore expect that recombinations are more important in the *rt-sph* than in the *rt-grid* simulation, in particular close to the ionising sources, i.e. for densities $n_H \gtrsim n_H^*$, where $n_H^* \equiv 10^{-1}$ cm^{-3} is the star formation threshold density (Sec. 6.2.1). We have indicated the star formation threshold density with the vertical dotted line in Fig. 6.1.

6.3 RESULTS

In this sections we present and discuss our results. We investigate the differences between the *rt-sph* simulation (which exploits the full dynamic range of the underlying spatially adaptive hydrodynamical simulation) and the *rt-grid* simulation (which employs only a fraction of the dynamic range of the hydrodynamical simulation by sampling the densities on a uniform grid) by comparing several key quantities.

We start by explaining differences in the evolution of the mean ionised fraction (Sec. 6.3.1). We then discuss differences in the morphologies of the ionised regions and in the topologies of reionisation as traced by the spatial distribution of the ionised gas and correlations between the ionised fraction and the gas density (Sec. 6.3.2). The product of neutral fraction and gas density determines the 21 cm brightness temperature of the hydrogen gas, one of the most important potential observables of reionisation. We will discuss differences in the statistical properties of this observable between the *rt-sph* and the *rt-grid* simulation by computing the power spectrum of the 21 cm brightness temperature fluctuations (Sec. 6.3.3).

In each of our comparisons we discuss similarities and differences between the results obtained in the *rt-sph* and the *rt-grid* simulation at fixed times or, equivalently, at fixed redshifts. In addition, we compare the results from the two simulations at fixed (volume-weighted) mean ionised fractions. In both simulations, the mean ionised fraction is a monotonically increasing function of time (Fig. 6.2). It therefore provides another unambiguous parametrisation of the
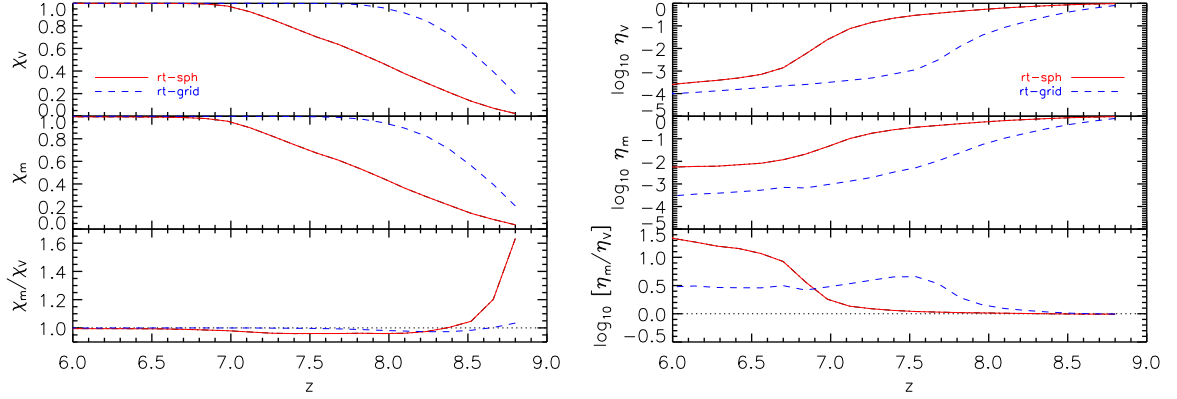
Figure 6.2: *Left-hand panel:* Evolution of the mean ionised fraction in the simulations *rt-sph* (red solid curves) and *rt-grid* (blue dashed curves). The panels show the volume-weighted (top) and mass-weighted (middle) means and their ratio (bottom). The RT simulations start at redshift $z = 8.94$ and the first data is saved at $z = 8.80$. At this point, the volume-weighted mean ionised fraction in *rt-grid* is already $\chi_V \approx 0.2$. In both simulations, reionisation starts inside-out ($\chi_m/\chi_V > 1$) and reverses to outside-in ($\chi_m/\chi_V < 1$). *Right-hand panel:* Same as left-hand panel, but for the mean neutral fraction to illustrate differences between *rt-sph* and *rt-grid* when $\chi_V \approx 1$.

reionisation history. We will point out that the two simulations should, however, really be compared at *both* fixed times *and* fixed ionised fractions. Although we leave such a comparison to future work, we will briefly explain how it could be accomplished.

6.3.1 Mean ionised fraction

Fig. 6.2 shows the evolution of the mean ionised (left) and neutral fraction (right) in the simulations *rt-sph* (red solid curves) and *rt-grid* (blue dashed curves). The individual panels show the volume-weighted means (top)

$$\chi_V \equiv \sum_i V_i \chi_i / \sum_i V_i \tag{6.3}$$

$$\eta_V \equiv \sum_i V_i \eta_i / \sum_i V_i, \tag{6.4}$$

the mass-weighted means (middle)

$$\chi_m \equiv \sum_i m_i \chi_i / \sum_i m_i \tag{6.5}$$

$$\eta_m \equiv \sum_i m_i \eta_i / \sum_i m_i \tag{6.6}$$

and their ratios (bottom). Here, $\chi_i \equiv n_{\mathrm{HII}}/n_{\mathrm{H}}$ is the ionised fraction of SPH particle i, $\eta_i \equiv n_{\mathrm{HI}}/n_{\mathrm{H}}$ is its neutral fraction, m_i is its mass and $V_i \equiv h_i^3$ is its characterstic volume.

At the end of the simulation, i.e. at redshift $z = 6$, the gas is highly ionised in both the *rt-sph* simulation and the *rt-grid* simulation, i.e. $\chi_m \approx \chi_V \approx 1$. The evolution of the mean ionised fractions from $z \approx 9$ to $z = 6$ in these two simulations is, however, very different. The transition

from the initial, fully neutral to the final, highly ionised regime occurs much more rapidly in the *rt-grid* than in the *rt-sph* simulation. The reason for this difference in the evolutions of the mean ionised fraction is that the number of recombinations that need to be overcome to keep the gas ionised is much larger in the *rt-sph* simulation than in the *rt-grid* simulation, a result of the increased small-scale clumpiness for high-density ($\log_{10} \Delta \gtrsim 2$) gas (see Fig. 6.1).

The ratio $\chi_{\rm m}/\chi_{\rm V}$ characterises the distribution of the ionised gas. To see this, let us assume for the moment that gas particles can either be fully ionised, i.e. $\chi_i = 1$, or fully neutral, ie. $\chi_i = 0$. Then (e.g., Iliev et al. 2006)

$$\frac{\chi_{\rm m}}{\chi_{\rm V}} \equiv \frac{\sum m_i \chi_i / \sum m_i}{\sum V_i \chi_i / \sum V_i} \tag{6.7}$$

$$= \frac{\sum_{\text{ionised particles}} m_i / \sum_{\text{all particles}} m_i}{\sum_{\text{ionised particles}} V_i / \sum_{\text{all particles}} V_i} \tag{6.8}$$

$$= \frac{1}{\langle \rho \rangle} \frac{M_{\text{ionised}}}{V_{\text{ionised}}}, \tag{6.9}$$

and the ratio $\chi_{\rm m}/\chi_{\rm V}$ is thus equal[7] to the mean density of the ionised gas in units of the mean gas density $\langle \rho \rangle$. Consequently, if $\chi_{\rm m}/\chi_{\rm V} > 1$, then overdense regions are preferentially ionised, and if $\chi_{\rm m}/\chi_{\rm V} < 1$, then underdense regions are preferentially ionised. The ratio $\chi_{\rm m}/\chi_{\rm V}$ is therefore commonly employed to characterise the topology of reionisation: if $\chi_{\rm m}/\chi_{\rm V} > 1$, then reionisation is said to proceed inside-out while it is said to proceed outside-in if $\chi_{\rm m}/\chi_{\rm V} < 1$.

In both the *rt-sph* simulation and the *rt-grid* simulation, $\chi_{\rm m}/\chi_{\rm V}$ decreases from $\chi_{\rm m}/\chi_{\rm V} > 1$ at early times to $\chi_{\rm m}/\chi_{\rm V} < 1$ at intermediate times and converges to $\chi_{\rm m}/\chi_{\rm V} \approx 1$ at late times. There are, however, clear difference in the evolution of $\chi_{\rm m}/\chi_{\rm V}$ predicted by the two simulations. The ratio of the mass-weighted to volume-weighted mean ionised fraction obtained from the *rt-sph* simulation is initially substantially larger than the one obtained from the *rt-grid* simulation. Moreover, the transition from $\chi_{\rm m}/\chi_{\rm V} > 1$ to $\chi_{\rm m}/\chi_{\rm V} < 1$ occurs significantly later in the *rt-sph* simulation than in the *rt-grid* simulation. Finally, at low redshifts ($z \lesssim 8.2$) the values for $\chi_{\rm m}/\chi_{\rm V}$ obtained from the *rt-sph* simulation remain systematically below the values for $\chi_{\rm m}/\chi_{\rm V}$ obtained from the *rt-grid* simulation.

We have compared the ratio $\chi_{\rm m}/\chi_{\rm V}$ obtained from the *rt-sph* simulation with the one obtained from the *rt-grid* simulation as a function of redshift. It is, however, also interesting to perform this comparison as a function of the mean ionised fraction. Indeed, a simple delay in the ionisation history due to an increased number of recombinations may in principle be compensated by an increase in the luminosities of the ionising sources, which are, both from a theoretical and from an observational point of view, still poorly constrained. Moreover, the hydrodynamical simulations employed here still lack the resolution (and large-scale dynamics) and physics to properly compute the fraction of ionising photons that are not used up by recombinations within the star-forming regions and hence manage to escape and ionise the intergalactic gas. Uncertainties in this *escape fraction* (e.g., Inoue, Iwata, & Deharveng 2006; Razoumov & Sommer-Larsen 2006; Gnedin, Kravtsov, & Chen 2008) are degenerate with the uncertainties in the source luminosities and hence may also be employed to compensate for a delay in the reionisation history.

In the left-hand panel of Fig. 6.3 we therefore compare the ratio $\chi_{\rm m}/\chi_{\rm V}$ obtained from the *rt-sph* simulation with the one obtained from the *rt-grid* simulation as a function of the volume-

---

[7]This equality is only approximate, because the SPH particle volumes do not tessellate space, i.e. $\sum_i V_i \neq L_{\rm box}^3$.
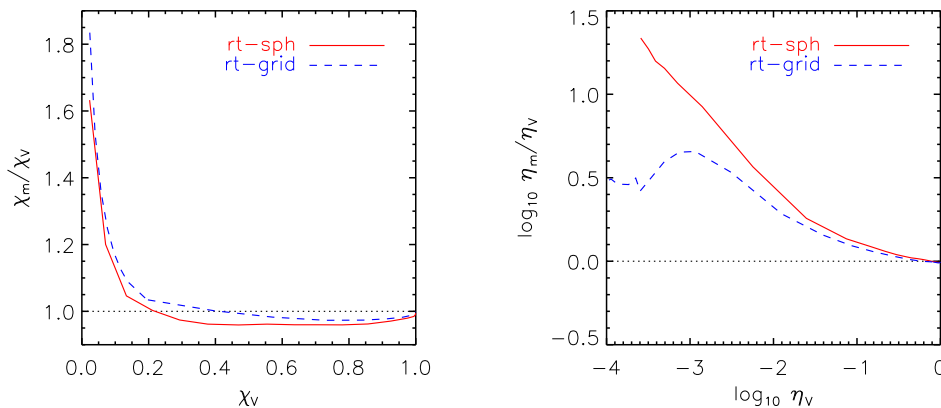
Figure 6.3: *Left-hand panel:* The ratio of mass-weighted to volume-weighted mean ionised fraction obtained from the *rt-sph* simulation (red solid curve) and the *rt-grid* simulation (blue dashed curve) as a function of the volume-weighted mean ionised fraction. The *rt-sph* simulation predicts a consistently lower ratio and hence a more marked outside-in reionisation topology than the *rt-grid* simulation. *Right-hand panel:* Same as left-hand panel, but for the mean neutral fractions to illustrate differences between *rt-sph* and *rt-grid* when $\chi_V \approx 1$.

weighted mean ionised fraction[8]. The *rt-sph* simulation predicts a reionisation history that is significantly more outside-in than the one predicted by the *rt-grid* simulation. This is likely due to the increased role of recombinations (and partly self-shielding / shadowing, see the next section) that keep the high-density gas in that simulation at larger neutral fractions. To illustrate the differences between the simulations for volume-weighted mean ionised fractions $\chi_V \approx 1$, we also show the ratio η_m/η_V of the mass-weighted mean neutral fraction $\eta_m = 1 - \chi_m$ and the volume-weighted mean neutral fraction $\eta_V = 1 - \chi_V$ as a function of η_V (right-hand panel of Fig. 6.3).

We caution the reader of the qualitative nature of our conclusions and that we only aim at highlighting differences between (the reionisation topologies obtained from) RT simulations that exploit the full dynamic range of the underlying hydrodynamical simulation (*rt-sph*) and those that do not (*rt-grid*). The simulations presented here use too small a box and too simplistic prescriptions for the ionising sources to be employed for predictions of the topology of reionisation. We will come back to this and other short-comings inherent to the present approach in our discussion in Sec. 6.4.

We finally note that reionisation simulations should ideally be compared at both fixed ionised fraction *and* fixed redshift (e.g., Lidz et al. 2008). Such a comparison would be particular preferable over comparisons performed at fixed redshift *or* fixed ionised fraction when studying the distribution of the ionised mass with respect to the total mass (Sec. 6.3.2) or when computing quantities that depend on both density and neutral fraction (Sec. 6.3.3). The comparison could be accomplished by tuning the luminosities of the ionising sources such as to yield a certain ionised fraction at a given redshift. Alternatively, one could perform RT simu-

---

[8]The volume-weighted mean ionised fraction at the first output of the *rt-grid* simulation is $\chi_V \approx 0.2$ (Fig. 6.2). To extend the ratio of mass-weighted to volume-weighted mean ionised fraction shown in the left-hand panel of Fig. 6.3 down to lower mean volume-weighted ionised fractions, we have resimulated part of the *rt-grid* simulation with more frequent outputs. We have, however, not included the results from this resimulation in Fig. 6.2.

lations on top of a single static snapshot at fixed redshift. Such simulations would clearly not be appropriate for studying the reionisation process as a whole, but they would facilitate the exposition of differences between corresponding RT simulations.

6.3.2   The morphology and the topology of ionised regions

In this section we discuss the morphology and the topology of the ionised regions predicted by the simulations *rt-sph* and *rt-grid*. We describe how the shapes of ionised regions and the spatial distribution of the ionised hydrogen mass evolve with time and we also point out differences in the evolution obtained from the two simulations. We present our results both as a function of redshift and as a function of mean volume-weighted ionised fraction.

Slices through the simulation box of the *rt-sph* and the *rt-grid* simulations are shown in the panels of the left-hand (*rt-sph*) and middle (*rt-grid*) columns of Figs. 6.4 and 6.5. While the panels in Fig. 6.4 show neutral fraction contours (and densities) at fixed redshift ($z = 8.80$, 8.38, 7.96, 7.54, 7.12 from top to bottom), the panels in Fig. 6.5 show neutral fraction contours (and densities) at fixed volume-weighted mean ionised fraction ($\chi_V = 0.2$, 0.4, 0.6, 0.8, 0.95 from top to bottom[9]). The slices were generated by mapping the SPH particles densities and neutral fractions to a uniform grid with $\tilde{N}_g = 128$ points per dimension using mass-conserving SPH interpolation. The contours show neutral fractions of $\eta = 0.5$ (blue), 0.05 (red) and 0.005 (green). When speaking of the morphology of ionised regions, we refer to the shape of the $\eta = 0.5$ contours. The grey-scale background image shows the gas overdensity Δ.

In both the *rt-sph* and the *rt-grid* simulation the first ionised regions appear around the densest structures, which correspond to the most massive halos hosting the first stellar sources of ionising radiation. The ionised regions quickly grow and combine to form a single ionised region that pervades the simulation box. The rapid formation of a single large ionised bubble is mostly a consequence of the relatively few ionising sources the simulations contain (Sec. 6.2.1). Inside the ionised bubble, there are regions where the gas is still substantially neutral. These are regions of very high density, where recombinations (partially) offset the ionisations due to the stellar radiation. In the densest regions, one may also expect to find the gas (partially) neutral because it is self-shielded (see the discussion below).

At fixed redshift (Fig. 6.4), the ionised regions in the *rt-grid* simulation are always larger than the ionised regions in the *rt-sph* simulation, which is simply a reflection of the different evolution of the mean ionised fraction in these simulations (Fig. 6.2). Likewise, when compared at fixed redshift, the simulations predict different topologies for the ionised gas: the *rt-sph* simulation displays substantially more substructure in the neutral fraction than the *rt-grid* simulation. To remove the large dependence of the results on the mean ionisation history, we compare the *rt-sph* and *rt-grid* simulations at fixed mean ionised fraction (Fig. 6.5). This is justified by the fact that a simple delay in the reionisation history is degenerate with uncertainties in the ionising luminosities and other quantities (see our discussion in Sec. 6.3.1).

The comparison at fixed mean ionised fraction paints a rather different picture. Both simulation now predict very similar shapes for the ionised regions, a finding that is in agreement with expectations from previous work (e.g., McQuinn et al. 2007). In the present case this can be understood by noting that the properties of the density fields employed in the *rt-sph* and the *rt-grid* simulation differ mainly at high densities, which correspond to regions that occupy only a small volume. The *rt-sph* simulation still predicts, however, substantially more substructure

---

[9]The actual values of the volume-weighted mean ionised fraction may fluctuate around the quoted values (within $\lesssim 5\%$), because the data was saved only at a finite number of redshifts.
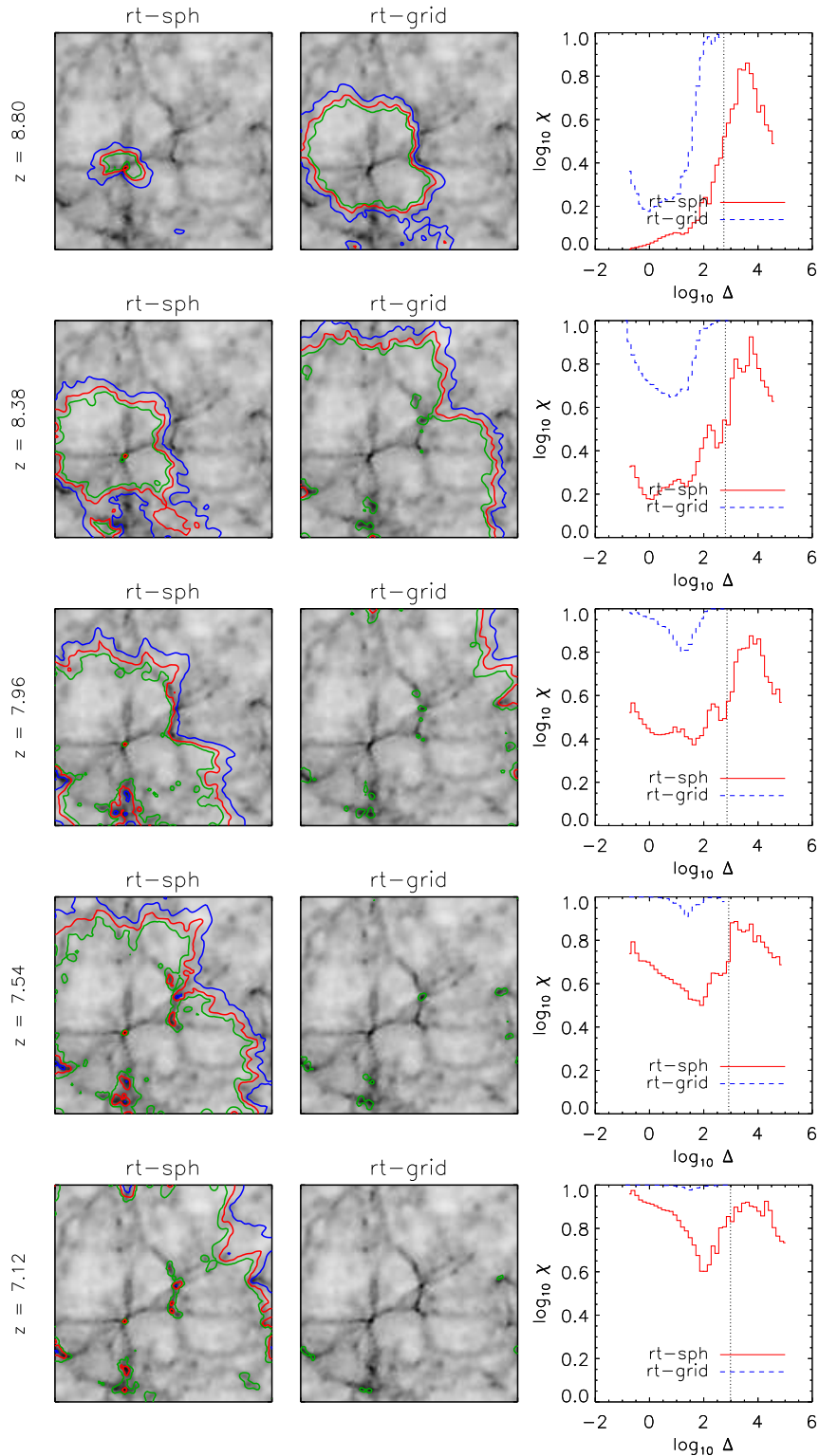
Figure 6.4: Morphology of ionised regions and topology of reionisation: evolution with redshift z. In each column, panels correspond to $z = 8.80, 8.38, 7.96, 7.54$, and 7.12 (from top to bottom). *Left-hand and middle column:* Slices through the centre of the *rt-sph* (left-hand column) and the *rt-grid* (middle column) simulation, as indicated in the panel titles. Contours show neutral fractions of $\eta = 0.5$ (blue), 0.05 (red) and 0.005 (green). *Right-hand column:* average (in logarithmic overdensity bins) ionised fraction for both the *rt-sph* (solid red histogram) and the *rt-grid* (dashed blue histogram) simulation. The vertical dotted lines indicate the (redshift-dependent) overdensity that corresponds to the (physical) star formation threshold hydrogen density $n_{\mathrm{H}}^* \equiv 10^{-1}$ cm^{-3} (Sec. 6.2.1). See text for a discussion.
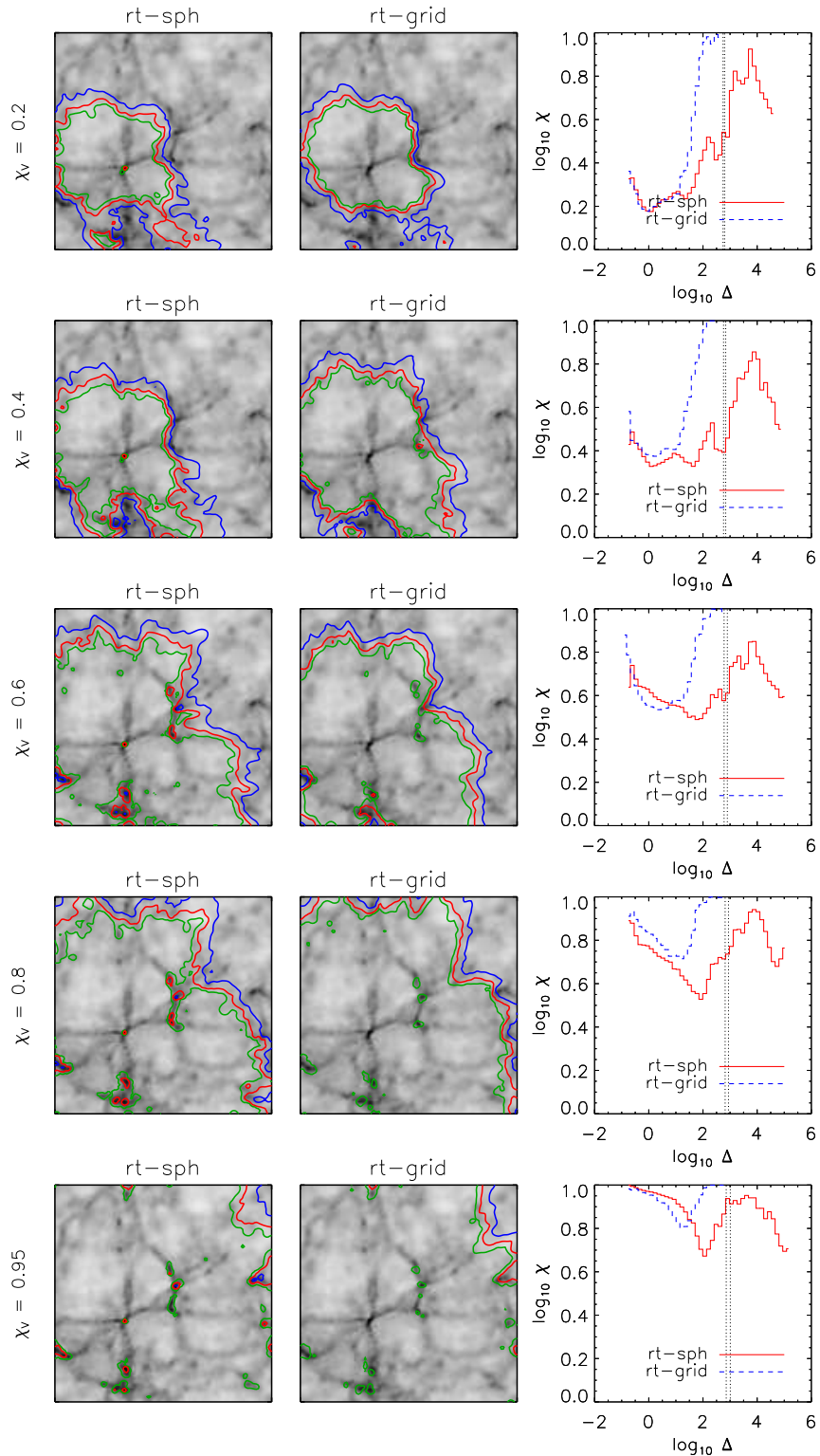
Figure 6.5: Morphology of ionised region and topology of reionisation: evolution with the volume-weighted mean ionised fraction χ_V. In each column, panels correspond to $\chi_V = 0.2, 0.4, 0.6, 0.8$ and 0.95 (from top to bottom). The left-most (right-most) vertical dotted lines indicate the (redshift-dependent) overdensity that corresponds to the (physical) star formation threshold hydrogen density $n_H^* \equiv 10^{-1}$ cm^{-3} (Sec. 6.2.1) in the simulation *rt-grid* (*rt-sph*). Otherwise, the figure is identical to Fig. 6.4.

in the distribution of the ionised mass than the *rt-grid* simulation. It is clear that the difference in substructure is due to the difference in the dynamic range. Its interpretation is, however, impeded by the fact that the same mean ionised fraction corresponds to different redshifts in the two simulations. Some of the differences may therefore just be due to difference in the gravitational growth of structure, as discussed in the previous section.

We now compare the reionisation topologies predicted by the simulations *rt-sph* and *rt-grid* in a more quantitative manner. The panels in the right-hand columns of Figs. 6.4 and 6.5 show the mean ionised fraction in logarithmic bins of overdensity, both for the *rt-sph* simulation (red solid histogram) and the *rt-grid* simulation (blue dashed histogram). It is immediately apparent that in both simulations the ionised fraction shows a strong dependence on overdensity.

Let us first discuss the dependence of the ionised fraction on overdensity and its evolution for the *rt-grid* simulation. The first stars form in the regions of the highest densities. These regions are therefore expected to become ionised first. Indeed, gas at overdensities $\log_{10} \Delta \sim 2$, which correspond to the largest overdensities present in the *rt-grid* simulation, is almost fully ionised, even at a volume-weighted mean ionised fraction as low as $\chi_V = 0.2$. The gas is also highly ionised in the most underdense regions, characterised by $\log_{10} \Delta \approx -1$.

For low volume-weighted mean ionised fractions, the particle ionised fractions at these low overdensities are on average somewhat smaller than those at overdensities $\log_{10} \Delta \sim 2$, because the ionised regions do not yet encompass a large fraction of the total volume of the underdense regions in the simulation. Instead, the ionisation fronts are still close to the dense regions that host the ionising sources. The ionised fractions at overdensities $\log_{10} \Delta \approx -1$ only become, on average, comparable to those at overdensities $\log_{10} \Delta \approx 2$ when the volume-weighted mean ionised fraction reaches $\chi_V \gtrsim 0.6$. There is a distinct depression in the ionised fraction at overdensities $0 \lesssim \log_{10} \Delta \lesssim 2$. Note that this depression remains visible even at redshift $z = 7.12$, i.e. long after reaching a volume-weighted mean ionised fraction of $\chi_V \approx 1$.

At fixed volume-weighted mean ionised fraction χ_V (Fig. 6.5) and for overdensities $\log_{10} \Delta \lesssim 1$ the ionised fractions in the *rt-sph* simulations are on average similar to those in the *rt-grid* simulation. The distinct depression in the ionised fraction at overdensities $0 \lesssim \log_{10} \Delta \lesssim 2$ present in simulation *rt-grid* is also visible here, and extends to somewhat larger overdensities. Due to the larger dynamic range, recombinations can efficiently counteract photo-ionisations closer to the ionising sources (and hence out to denser regions) than in the *rt-grid* simulation.

Overdensities $\log_{10} \Delta > 3$ are only present in the *rt-sph* simulation. The gas in these regions shows a complex dependence of the ionised fraction on the overdensity. For overdensities $3 \lesssim \log_{10} \Delta \lesssim 4$, the ionised fraction generally increases with overdensity. This is probably because regions of larger overdensity will generally be located closer to ionising sources and hence experience a larger photo-ionisation rate. This general trend is, however, interrupted by several reversals. For overdensities $\log_{10} \Delta > 4$, i.e. for the largest overdensities in the simulation, the ionised fraction decreases with overdensity. Since regions of such high overdensities are almost certain to host (many) ionising sources, it is likely that this decrease is caused by the increased importance of recombinations at these overdensities.

Some of the high-density gas in the *rt-sph* simulation may also remain substantially neutral because it is (partly) self-shielded. The criterion for self-gravitating gas clouds to self-shield is (Schaye 2001) $n_H^{\text{self}} \gtrsim 10^{-1}$ cm$^{-3}(\Gamma/10^{-12}$ s$^{-1})$, where Γ is the hydrogen photo-ionisation rate. The critical hydrogen density n_H^{self} above which self-shielding may become important corresponds to a critical gas overdensity Δ^{self} of

$$\Delta^{\text{self}} \gtrsim 10^3 \left(\frac{1+z}{7} \right)^{-3} \left(\frac{\Gamma}{10^{-12} \text{ s}^{-1}} \right). \tag{6.10}$$

Unfortunately, we have not tracked the photo-ionisation rate in the current simulations. For now, lets simply assume that the photo-ionisation rate is roughly of the order of the photo-ionisation rate found in simulations reported by other authors, $\Gamma \sim 10^{-12}$ s^{-1} (e.g., Mesinger & Dijkstra 2008; Choudhury, Haehnelt, & Regan 2009). This assumption may be justified by noting that the *rt-sph* simulation shows a reionisation history whose duration is similar to that found there. Eq. 6.10 then suggests that self-shielding may be partly responsible for the depression in the ionised fraction in the densest regions. We note that Eq. 6.10 also implies that self-shielding is unimportant in the *rt-grid* simulation, where the overdensities do not exceed values of $\log_{10} \Delta = 3$.

A similar study of the density-dependence of the ionised fraction and the effects of recombinations was presented in the semi-analytical work of Choudhury, Haehnelt, & Regan (2009). Our general conclusions about the importance of recombinations are in qualitative agreement with theirs. There are, however, also differences. Most notably, in their simulations photo-ionisations always manage to overcome the effect of recombinations in the densest regions corresponding to the most massive halos, keeping the gas highly ionised. Note, however, that Choudhury, Haehnelt, & Regan (2009) only considered gas overdensities up to $\log_{10} \Delta = 1$. We mention that Choudhury, Haehnelt, & Regan (2009) used simulation boxes of size $100 \ h^{-1}$ Mpc, much larger than the one used here, and that they employed different prescriptions for obtaining the gas densities and placing the ionising sources. We will repeat our analysis using larger simulation boxes and different source prescriptions to allow for a more honest comparison to Choudhury, Haehnelt, & Regan (2009) in future work. We hope to improve on their work as our simulations not only employ a more accurate description of the gas distribution at small scales but also account for the effects of shadowing and self-shielding that their semi-analytical approach necessarily ignored.

The dependence of the ionised fraction on density was also studied by Iliev et al. (2006), who performed RT simulations on top of very high-resolution DM simulations. Their simulations were performed using box sizes up to $100 \ h^{-1}$ Mpc with a DM particle mass of 2.5×10^7 M$_\odot$ and constitute some of the largest and most accurate RT reionisation simulations carried out to date. However, the densities of the DM simulation, after translating them into gas densities using the cosmic baryon fraction, were interpolated to a grid with only 203^3 points for their default RT simulations, which corresponds to a relatively low spatial resolution of $\approx 0.5 \ h^{-1}$ Mpc. The corresponding low dynamic range may explain why Iliev et al. (2006) find a much less pronounced effect of inhomogeneous recombinations (and self-shielding) than found in Choudhury, Haehnelt, & Regan (2009) and in the present study.

In summary, in this section we studied the morphology of ionised regions and the topology of reionisation in the *rt-sph* and the *rt-grid* simulations and compared them with each other. In agreement with previous work, when compared at fixed volume-weighted mean ionised fraction we found similar morphologies of the ionised regions in both simulations, despite the large difference in the dynamic range they exhibit. There are, however, large differences in the ionisation state of high-density ($\log_{10} \Delta \gtrsim 1$) gas, even when compared at fixed ionised fraction. In the (spatially adaptive) *rt-sph* simulation, recombinations are much more likely to overcome the effect of photo-ionisations than in the *rt-grid* simulation.

We emphasise that the current study should only be considered as preliminary, due to our use of a comparatively small simulation box and simplified prescriptions for the ionising sources. We will present simulations using larger box sizes and different source prescriptions in future work.

6.3.3 Statistical analysis - 21 cm power spectrum

The redshifted 21 cm signal emitted by neutral hydrogen atoms provides a potential probe of the epoch of reionisation and several radio telescopes are currently being planned and constructed to detect it. Radio surveys targeting the 21 cm signal promise to open a previously unexplored observational window onto reionisation by providing a three-dimensional tomographic view of the intergalactic gas in the high-redshift Universe.

Direct imaging of neutral regions during reionisation will require observatories like SKA and FTTE (Tegmark & Zaldarriaga 2009) which are still being developed and which will probably only become operational in one or two decades. Statistical probes of the high-redshift Universe in 21 cm will, however, already be possible within the next few years with radio interferometers like LOFAR, MWA and 21CMA[10] whose construction is nearly complete. One of the most promising statistical probes is provided by the 21 cm power spectrum, which we will therefore briefly discuss.

The 21 cm signal is formed by the spin-flip transition of neutral hydrogen. It may be detected by measuring the differential 21 cm brightness temperature T_{21} with respect to the Cosmic Microwave Background (CMB), which is determined by the density $n_{\mathrm{HI}} = \eta n_{\mathrm{H}}$ of neutral hydrogen and its spin temperature T_{s}. It is given by (e.g., Furlanetto, Oh, & Briggs 2006)

$$T_{21} = \frac{T_{\mathrm{s}} - T_{\mathrm{CMB}}}{1 + z} \left(1 - e^{-\tau} \right), \qquad (6.11)$$

where $T_{\mathrm{CMB}} = 2.73\ \mathrm{K}(1 + z)$ is the temperature of the CMB at redshift z (Fixsen et al. 1996), and τ is the 21 cm optical depth. In the Gunn-Peterson approximation (Gunn & Peterson 1965; see, e.g., Furlanetto, Oh, & Briggs 2006 for its application to the 21 cm transition),

$$\tau(z) = \frac{3 h_{\mathrm{p}} c^3 A_{21} n_{\mathrm{HI}}(z)}{32 \pi k_{\mathrm{B}} T_{\mathrm{s}}(z) H(z) \nu_{21}^2}, \qquad (6.12)$$

where $\nu_{21} = 1420.4\ \mathrm{MHz}$ is the rest-frame frequency of the spin-flip transition (corresponding to a wavelength of 21.1 cm), $A_{21} = 2.84 \times 10^{-15}\ \mathrm{s}^{-1}$ is the Einstein coefficient for spontaneous emission, k_{B} is the Boltzmann constant, h_{p} is the Planck constant, c is the speed of light and $H(z)$ is the Hubble constant at redshift z. Assuming $\tau \ll 1$, which is correct for the redshifts of interest here except for some lines of sight through mini-halos (Mellema et al. 2006; Iliev et al. 2002), Eqs. 6.11 and 6.12 yield

$$T_{21} \approx 28\ \mathrm{mK}\ \eta \Delta \left(1 - \frac{T_{\mathrm{CMB}}}{T_{\mathrm{s}}} \right) \left(\frac{1 + z}{10} \right)^{1/2}, \qquad (6.13)$$

where we have furthermore assumed that the hydrogen number density in units of the cosmic mean hydrogen number density is given by the gas overdensity, i.e. we have assumed that the hydrogen abundance X is constant, and we have employed the high-redshift approximation of the Hubble constant $H(z) \approx H_0 \Omega_{\mathrm{m}}^{1/2}(1 + z)^{3/2}$.

The spin temperature, which characterises the population of the energy levels that correspond to the 21 cm transition, is determined by the statistical equilibrium of collisional excitations and de-excitations by hydrogen atoms and electrons and radiative excitations and de-excitations by cosmic microwave background and Lyman$-\alpha$ photons (Field 1959). For many applications it is a good approximation to assume that the spin temperature is much larger than

---

[10]http://21cma.bao.ac.cn

the CMB temperature, $T_{\rm s} \gg T_{\rm CMB}$ (e.g., Ciardi & Salvaterra 2007). The brightness temperature then becomes independent of $T_{\rm s}$,

$$T_{21} \approx 28 \text{ mK } \eta\Delta \left(\frac{1+z}{10}\right)^{1/2}. \tag{6.14}$$

The 21 cm power spectrum $P_{21}(\mathbf{k})$ at wave vector $\mathbf{k}$ is defined as (e.g., Furlanetto, Oh, & Briggs 2006)

$$P_{21}(\mathbf{k}) = \langle |\hat{T}_{21}(\mathbf{k})|^2 \rangle, \tag{6.15}$$

where the angular brackets denote an ensemble average and

$$\hat{T}_{21}(\mathbf{k}) = \int d\mathbf{r}\, e^{-i\mathbf{k}\mathbf{r}} T_{21}(\mathbf{r}) \tag{6.16}$$

$$\approx 28 \text{ mK } \left(\frac{1+z}{10}\right)^{1/2} \int d\mathbf{r}\, e^{-i\mathbf{k}\mathbf{r}} \eta(\mathbf{r})\Delta(\mathbf{r}) \tag{6.17}$$

is the Fourier transform of the differential brightness temperature T_{21}.

For the numerical estimation of the power spectrum we follow the description in Press et al. 1992, to which we refer the reader for details. Briefly, we start by assigning the neutral hydrogen masses of the SPH particles to a uniform grid with $\tilde{N}_{\rm g} = 128$ points per dimension using mass-conserving SPH interpolation. From the gridded densities and neutral fractions we obtain the 21 cm brightness temperature using Eq. 6.14. We use the FFTW library[11] to obtain the Fourier transform $\hat{T}_{21}(\mathbf{k})$ at discrete values of the wave vector $\mathbf{k} \equiv (k_x, k_y, k_z) = (i, j, k)k_{\rm Ny}/\tilde{N}_{\rm g}$, where i, j, k are integers that range from $-\tilde{N}_{\rm g}$ to $\tilde{N}_{\rm g}$ and $k_{\rm Ny} = \pi\tilde{N}_{\rm g}/L_{\rm box}$ the Nyquist frequency, which corresponds to the largest wave vector that is sampled by the employed grid. We then compute the periodogram estimate of the 21 cm power spectrum $P_{21}(\mathbf{k}) = |\hat{T}_{21}(\mathbf{k})|^2$. Finally, we average $P_{21}(\mathbf{k})$ in spherical bins to obtain the one-dimensional power spectrum estimate $P_{21}(k)$.

Fig. 6.6 shows the evolution of the 21 cm power spectra obtained from the *rt-sph* (left-hand panels) and the *rt-grid* (right-hand panels) simulation. The top and bottom panels show the evolution of the power spectra with redshift and ionised fraction, respectively. In each panel, the left and right solid vertical line indicates, respectively, the size of the simulation box $L_{\rm box}$ and the Nyquist scale $2\pi/k_{\rm Ny}$. The finite size of the simulation box, as well as the finite size of the grid employed to sample it, restricts our discussion to scales larger than the Nyquist scale[12] and smaller than the size of the simulation box.

The evolution of the 21 cm power spectrum depends on the details of the reionisation transition and hence is generally sensitive to the employed reionisation model. Some of its features are, however, generic to a large number of models (Lidz et al. 2008) and we summarise them here (see Furlanetto, Oh, & Briggs 2006 for an extensive review). Before reionisation, the 21 cm power spectrum of the neutral hydrogen gas is simply proportional to the power spectrum of the hydrogen density. At large scales, where linear theory is valid and the gaseous matter traces

---

[11]http://www.fftw.org/

[12]Due to the mass assignment onto the grid, the power spectrum may already be misrepresented at significantly larger scales and should therefore be deconvolved with an appropriate window function (Jing 2005) or computed using a mass assignment function that minimises artefacts (Cui et al. 2008). We have made no attempt to deconvolve the power spectrum to correct for the fact that the neutral hydrogen density field used in the computations is, due to our use of transmissive simulation box boundaries, not periodic, and hence constitutes only part of an infinitely large volume (e.g., Schlittgen & Streitberg 2001).
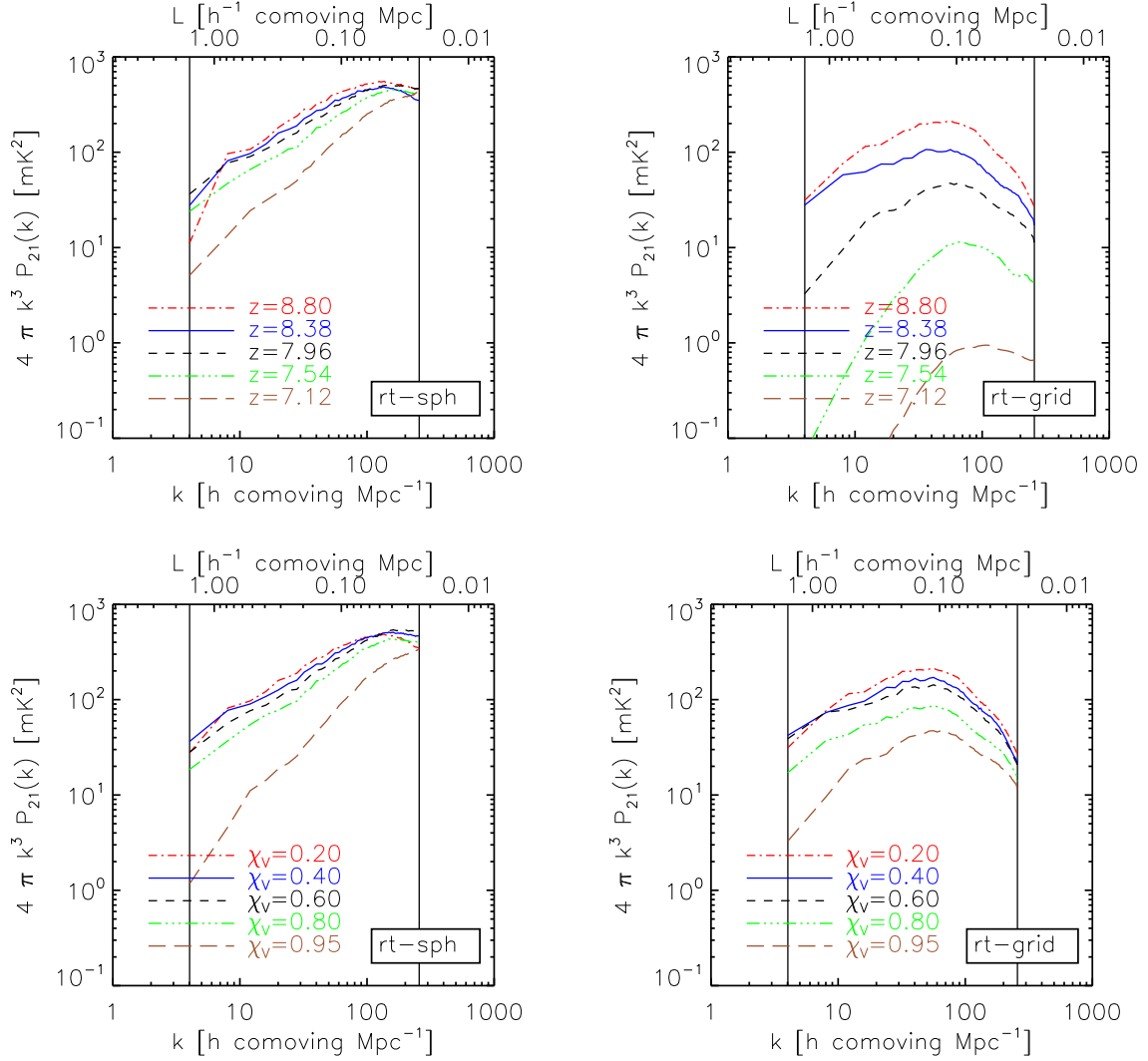
Figure 6.6: Evolution of the 21 cm power spectrum with redshift (top row) and ionised fraction (bottom row) for the simulations *rt-sph* (left-hand column) and *rt-grid* (right-hand column). In each panel, the right-hand solid vertical line indicates the Nyquist scale $2\pi/k_{\mathrm{Ny}}$ and the left-hand solid vertical line indicates the size of the simulation box L_{box}.

the DM content of the Universe, the shape of the 21 cm power spectrum therefore resembles that of the well-known linear theory DM power spectrum at this time.

The growth of ionised regions during reionisation leads to a decrease in the 21 cm power spectrum amplitude at scales smaller than their typical size, where the gas is mostly ionised and hence the neutral fraction is very low, and an increase in the power spectrum on scales larger than that. Some models of stellar reionisation even predict a distinct bump in the 21 cm power spectrum at scales corresponding to the typical size of the ionised regions (e.g., Furlanetto, Zaldarriaga, & Hernquist 2004). The 21 cm power spectrum reaches its maximum amplitude at $\chi_{\mathrm{V}} \approx 0.5$, when the individual ionised regions start to overlap (Lidz et al. 2008). Towards the end of reionisation ($\chi_{\mathrm{V}} \gtrsim 0.9$) the amplitude of the 21 cm power spectrum rapidly decreases as

the mean neutral fraction drops to zero. Despite this decrease in amplitude the 21 cm power spectrum may still be measurable at lower redshifts (Loeb & Wyithe 2008), since the contamination by galactic foreground signals, which poses the largest challenge for its detection, scales with redshift as $(1 + z)^{2.6}$.

Both the simulations *rt-sph* and *rt-grid* predict qualitatively similar evolutions for the 21 cm power spectra, which are in close agreement with the discussion above. The overall amplitude of the power spectrum obtained from *rt-grid* evolves, however, much more rapidly with redshift than that obtained from *rt-sph*. This is mostly due to the fact that the mean ionised fraction evolves much more rapidly for *rt-grid* (Fig. 6.2), a direct consequence of the difference in the dynamic range exhibited by the two simulations (Sec. 6.2.3). Indeed, the overall amplitudes of the power spectra predicted by the *rt-sph* and the *rt-grid* simulation evolve on more similar time scales when compared as a function of mean (volume-weighted) ionised fraction, a fact that has also been noticed by other authors (e.g., Lidz et al. 2008).

On small scales, the amplitude of the power spectrum from the *rt-sph* simulation is much higher than the one from the *rt-grid* simulation. The difference in the power spectra at these scales is a direct consequence of the difference in the dynamic ranges probed by the simulations. Its interpretation is complicated by the fact that the 21 cm power spectrum is proportional to the product of the density and the neutral fraction (and also depends on redshift). It would therefore be helpful to compare the power spectra obtained from the *rt-sph* and the *rt-grid* simulation at *both* the same redshifts *and* the same mean ionised fractions. We have outlined earlier how such a comparison could be accomplished (Sec. 6.3.1). Moreover, it would be desirable to compare the differences between the 21 cm power spectra from the *rt-sph* and the *rt-grid* simulation to the differences between the corresponding hydrogen density and ionised fraction power spectra, to disentangle their contributions.

In summary, in this section we employed the *rt-sph* and the *rt-grid* simulation to compute the 21 cm power spectrum, one of the most promising future observational probes of reionisation. We found that the power spectra in both these simulations evolve in qualitative agreement with expectations from previous work. A direct comparison of the 21 cm power spectra obtained from the *rt-sph* and the *rt-grid* simulation, both at fixed redshifts and at fixed mean ionised fractions, revealed, however, significant differences, which we explained by the difference in the dynamic ranges probed. The presence of these differences illustrates the importance of performing spatially adaptive RT simulations that exploit the full dynamic range exhibited by state-of-the-art cosmological hydrodynamical simulations.

We acknowledge the preliminary character of the present work and emphasise the need to repeat the present analysis using a set of simulations that employ a range of box sizes and mass resolutions to enlarge the range of scales probed and to study the convergence of the results. Note that much larger simulation boxes are also required because interferometers observe the 21 cm signal through a beam that smoothes the power on angular scales of several arc minutes, corresponding to scales as large as several comoving Mpc over the redshift range of interest (e.g., Valdés et al. 2006; Mellema et al. 2006; Zaldarriaga, Furlanetto, & Hernquist 2004). Our results are also certainly affected by the small number of ionising sources and our simplified assumptions about their properties: in our simulations, the initial phase of reionisation that is characterised by the presence of many non-overlapping ionised regions, is largely skipped. By employing the Gunn-Peterson approximation to compute the 21 cm optical depth we have furthermore ignored the thermal broadening of the 21 cm spectral line and we also did not account for redshift space distortions (Kaiser 1987). We discuss more caveats of the present study in our conclusions, which we present next.

6.4   Conclusions

Radiative transfer (RT) simulations coupled to hydrodynamical models of the early Universe are one of the most promising techniques to study the epoch of reionisation, an important milestone in the history of our Universe. Simulating reionisation is a computationally demanding task that requires the hydrodynamical modelling of representative volumes of the Universe at very high resolution. Many RT simulations are, however, performed using relatively coarse, uniform grids. Many simulations also ignore the hydrodynamics and perform the RT on top of N-body simulations, assuming the gas to trace the dark matter.

It has, however, been pointed out that the modelling of the gas on small scales may crucially affect the predictions for the topology of reionisation. Because the first stars form in the densest regions, it is expected that reionisation starts from the inside out, with the gas in the halos that host the stars being ionised prior to the gas in the voids further away. The detection of Lyman-limit systems in the spectra of high redshift quasars, on the other hand, suggests that towards the end, reionisation proceeds outside-in, with the ionising radiation eating its way from the voids into remaining (partially) neutral regions of high density. The phase of outside-in reionisation is, however, not predicted by many of the current generations of RT simulations.

Here we performed spatially adaptive RT simulations on top of cosmological Smoothed Particle Hydrodynamics (SPH) simulations to study the epoch of reionisation. We compared these simulations with RT simulations that were performed on top of density fields obtained by mapping the SPH densities to a uniform grid. The two types of simulations were designed to investigate the importance of exploiting the full dynamic range available in the underlying hydrodynamical simulation.

Our RT simulations employed TRAPHIC (Chapter 4; Pawlik & Schaye 2008), a RT scheme that has been specifically designed for use with large SPH simulations. Its advantages are that it works directly on the SPH particles of the hydrodynamical simulation, that it is spatially adaptive and that its computation time does not scale with the number of sources. In addition, it is parallelised for use with distributed memory machines. TRAPHIC can be used to solve the time-dependent RT equation in step with the hydrodynamical evolution. Here we have, however, solved the time-independent RT equation by post-processing static density fields. We did this to facilitate the interpretation of our results and their comparison with previous work.

We first discussed the evolution of the mass- and volume-weighted mean ionised fractions obtained from our simulations. Due to the larger average recombination rate, the RT simulation performed on the original SPH density field predicted a much slower and more gradual evolution in the mean ionised fractions than the RT simulation that used the gridded density field. In both simulations the ratio of the mass-weighted and the volume-weighted mean ionised fractions evolved from values larger than one in the beginning of the simulation to values smaller than one towards its end. This shows that, at least globally, in both simulations reionisation first proceeds inside-out, with the ionising radiation propagating from the high-density star-forming regions into the low-density large-scale voids, before switching to outside-in, from the highly ionised voids into the remaining (partially) neutral regions of high density. The outside-in phase is, however, more marked in the RT simulation that was performed on the original spatially adaptive density field than in the one that was performed on the gridded density field (when compared at fixed mean ionised fraction).

We found that, in agreement with previous work, the morphology of ionised regions is, in contrast to their topology, largely unaffected when the dynamic range is increased. To further investigate the topology of reionisation, we studied the dependence of the ionised fraction on

the density of the gas. We found that locally the evolution of the topology of the ionised gas cannot be characterised by a simple sequence of inside-out followed by outside-in reionisation. Instead, the ionised fraction is a complex function of the gas overdensity. For sufficiently high mean ionised fractions, the highest ionised fractions are generally found in the low-density voids and the high-density star-forming regions.

The ionised fraction shows a prominent depression at overdensities $\log_{10} \Delta \sim 2$ ($\log_{10} \Delta \sim 1$) in the simulations using the original (gridded) density fields. At both lower and higher densities, the recombination rate is too low to significantly overcome the ionising effect of the stellar radiation. The depression occurs at higher overdensities in the simulation employing the original gas density field, because the increased dynamic range increases the clumping factor and hence recombinations may overcome ionisations closer to the sources. In the simulations employing the gridded density fields the highest density gas ($\log_{10} \Delta \sim 3$) is always highly ionised. The dependence of the ionised fraction on density in the simulations employing the original density fields shows a more complex behaviour. For overdensities $3 \lesssim \log_{10} \Delta \sim 4$, the ionised fraction generally increases, but may exhibit several depressions similar to (but less pronounced than) that at overdensities $\log_{10} \Delta \sim 2$. For overdensities $\log_{10} \Delta > 4$, the ionised fraction generally decreases with overdensity.

Finally, we discussed the power spectrum of 21 cm brightness temperature fluctuations, which is one of the most important potential observables of the reionisation epoch. We found its general evolution to be consistent with expectations from previous work. The 21 cm power spectrum first traces the linear cold dark matter power spectrum with modifications on small scales due to the appearance of the first ionised regions. The power is shifting from small to large scales as the ionised regions grow and finally diminishes as most of the volume of the Universe becomes ionised. The simulation that was performed on the original SPH density field predicted significantly more power on small scales than the simulation that was performed on the gridded density field, as expected from the differences in the dynamic range. The interpretation of this enhanced small-scale power is, however, complicated by the fact that the 21 cm brightness temperature is proportional to the product of both density and neutral fraction and also depends on redshift.

We caution the reader that the hydrodynamical simulations that we have employed as part of the present pilot study have likely not yet converged. Although all of our simulations employ a sufficiently high resolution to resolve all halos with virial temperatures $T_{\mathrm{vir}} \gtrsim 10^4$ K with at least 100 particles, none of them has the resolution to predict the properties of the multiphase medium associated with the star-forming regions that these halos host. Furthermore, our use of a comparatively small box size leads us to underestimate the effects of large-scale structure formation on the small-scale clumpiness of the cosmic gas and biases the halo mass function away from its expected values. The mass of the most massive dark matter halos that the present simulations are able to host cannot exceed $\sim 10^{11} \ h^{-1} \ \mathrm{M}_\odot$, corresponding to the total mass in the simulation box. Simulations with box sizes of $30 \ h^{-1}$ Mpc and larger will be required to obtain representative models of the Universe for use with RT simulations of reionisation (Barkana & Loeb 2004; Iliev et al. 2006).

As a result, the employed star formation rates have likely not converged. We have made no attempt to match observational constraints on the star formation rate (e.g., Hopkins & Beacom 2006). Instead, we have roughly rescaled the ionising luminosities of the stellar sources to accomplish reionisation in the *rt-sph* simulation by redshift $z = 6$. We expect that a convergence in the star formation rate is generally difficult to achieve, even when simulating representative volumes of the Universe at high-resolution. This is because the star formation rate depends on

a number of physical processes that our analysis ignored, some of which are mentioned below.

Our simulations did not include the radiation-hydrodynamical feedback from photo-heating that is known to significantly affect the clumpiness of the gas in star-forming regions and the intergalactic medium (e.g., Haiman, Abel, & Madau 2001; Oh & Haiman 2003; Wise & Abel 2005; Pawlik, Schaye, & van Scherpenzeel 2009a). Photo-heating evaporates the gas out of low mass halos and decreases the average recombination rate in the intergalactic gas through Jeans filtering (e.g. Shapiro, Giroux, & Babul 1994; Gnedin & Hui 1998; Okamoto, Gao, & Theuns 2008). It moreover lowers the efficiency of gas to cool and hence impedes its accretion onto halos of all masses (Efstathiou 1992). The feedback from photo-heating may, moreover, be amplified by feedback from supernova explosions (Pawlik & Schaye 2009b), which we have also ignored.

Because we have assumed the presence of a photo-dissociating background, the formation of molecular hydrogen is suppressed in our simulations. In reality, the gas may contain a significant fraction of molecular hydrogen before reionisation (but see, e.g., Haiman, Rees, & Loeb 1997). Star formation and the associated kinetic feedback would then already be efficient in halos with virial temperatures much smaller than 10^4 K (e.g., Tegmark et al. 1997). We have also ignored the existence of atoms and ions heavier than helium. Supernova explosions may, however, quickly enrich the interstellar and intergalactic gas with metals (e.g., Bromm, Yoshida, & Hernquist 2003), which would increase its ability to cool. In our simulation the gas in halos with virial temperatures $< 10^4$ K is therefore biased to be ionised from the outside in.

These caveats are, however, unlikely to affect our qualitative conclusions derived from our comparisons of RT simulations that employ spatially adaptive density fields with RT simulations that employ density fields interpolated to a uniform grid. Our work therefore underlines the important role played by small-scale gas inhomogeneities in large-scale cosmological simulations of reionisation.

ACKNOWLEDGEMENTS

REFERENCES

Alvarez M. A., Bromm V., Shapiro P. R., 2006, ApJ, 639, 621

Barkana R., Loeb A., 2001, PhR, 349, 125

Barkana R., Loeb A., 2004, ApJ, 609, 474

Bromm V., Yoshida N., Hernquist L., 2003, ApJ, 596, L135

Bruzual G., Charlot S., 2003, MNRAS, 344, 1000

Choudhury T. R., 2009, arXiv, arXiv:0904.4596

Choudhury T. R., Haehnelt M. G., Regan J., 2009, MNRAS, 394, 960

Ciardi B., Stoehr F., White S. D. M., 2003, MNRAS, 343, 1101

Ciardi B., Ferrara A., 2005, SSRv, 116, 625

Ciardi B., Salvaterra R., 2007, MNRAS, 381, 1137

Cui W., Liu L., Yang X., Wang Y., Feng L., Springel V., 2008, ApJ, 687, 738

Efstathiou G., 1992, MNRAS, 256, 43P

Fan X., Carilli C. L., Keating B., 2006, ARA&A, 44, 415

Field G. B., 1959, ApJ, 129, 536

Finlator K., Özel F., Davé R., 2009, MNRAS, 393, 1090

Fixsen D. J., Cheng E. S., Gales J. M., Mather J. C., Shafer R. A., Wright E. L., 1996, ApJ, 473, 576

Furlanetto S. R., Zaldarriaga M., Hernquist L., 2004, ApJ, 613, 1

Furlanetto S. R., Oh S. P., 2005, MNRAS, 363, 1031

Furlanetto S. R., Oh S. P., Briggs F. H., 2006, PhR, 433, 181

Gnedin N. Y., Ostriker J. P., 1997, ApJ, 486, 581

Gnedin N. Y., Hui L., 1998, MNRAS, 296, 44

Gnedin N. Y., 2000, ApJ, 535, 530

Gnedin N. Y., Kravtsov A. V., Chen H.-W., 2008, ApJ, 672, 765

Gunn J. E., Peterson B. A., 1965, ApJ, 142, 1633

Haiman Z., Rees M. J., Loeb A., 1997, ApJ, 476, 458

Haiman Z., Abel T., Madau P., 2001, ApJ, 551, 599

Hopkins A. M., Beacom J. F., 2006, ApJ, 651, 142

Iliev I. T., Shapiro P. R., Ferrara A., Martel H., 2002, ApJ, 572, L123

Iliev I. T., Mellema G., Pen U.-L., Merz H., Shapiro P. R., Alvarez M. A., 2006, MNRAS, 369, 1625

Inoue A. K., Iwata I., Deharveng J.-M., 2006, MNRAS, 371, L1

Jing Y. P., 2005, ApJ, 620, 559

Kaiser N., 1987, MNRAS, 227, 1

Kennicutt R. C., Jr., 1998, ApJ, 498, 541

Kohler K., Gnedin N. Y., Hamilton A. J. S., 2007, ApJ, 657, 15

Komatsu E., et al., 2008, preprint (arXiv:0803.0547)

Lee K.-G., Cen R., Gott J. R. I., Trac H., 2008, ApJ, 675, 8

Lidz A., Zahn O., McQuinn M., Zaldarriaga M., Hernquist L., 2008, ApJ, 680, 962

Loeb A., Ferrara A., Ellis R. S., 2008, First Light in the Universe (Springer),

Loeb A., Wyithe J. S. B., 2008, PhRvL, 100, 161301

McQuinn M., Lidz A., Zahn O., Dutta S., Hernquist L., Zaldarriaga M., 2007, MNRAS, 377, 1043

Mellema G., Iliev I. T., Pen U.-L., Shapiro P. R., 2006, MNRAS, 372, 679

Mesinger A., Furlanetto S., 2007, ApJ, 669, 663

Mesinger A., Dijkstra M., 2008, MNRAS, 390, 1071

Miralda-Escudé J., Haehnelt M., Rees M. J., 2000, ApJ, 530, 1

Nakamoto T., Umemura M., Susa H., 2001, MNRAS, 321, 593

Oh S. P., Haiman Z., 2003, MNRAS, 346, 456

Okamoto T., Gao L., Theuns T., 2008, preprint (arXiv:0806.0378)

Pawlik A. H., Schaye J., 2008, MNRAS, 389, 651

Pawlik A. H., Schaye J., van Scherpenzeel E., 2009, MNRAS, 394, 1812

Pawlik A. H., Schaye J., 2009, MNRAS, L228

Press W. H., Teukolsky S. A., Vetterling W. T., Flannery B. P., 1992, Numerical recipes in C. The art of scientific computing, Cambridge University Press, 2nd ed.

Razoumov A. O., Sommer-Larsen J., 2006, ApJ, 651, L89

Schaye J., 2001, ApJ, 559, 507

Schaye J., 2004, ApJ, 609, 667
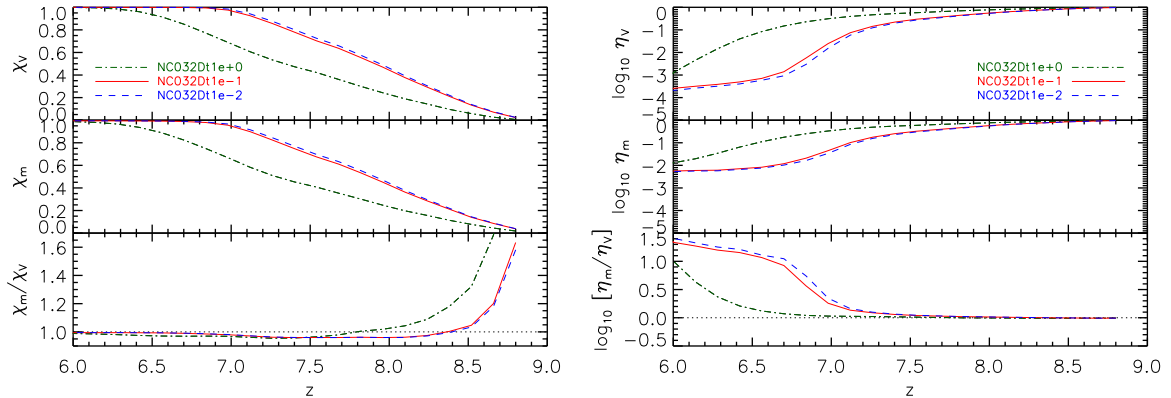
Figure 6.7: Numerical convergence study: RT time step. The evolution of the the mean ionised (left-hand panel) and the mean neutral (right-hand panel) fraction as obtained in the simulation *rt-sph* (red solid curves), which employed an angular resolution $N_c = 32$ and a time step $\Delta t_r = 10^{-1}$ Myr, is compared to those obtained from identical simulations but using time steps $\Delta t_r = 1$ Myr (green dot-dashed curves) and $\Delta t_r = 10^{-2}$ Myr (blue dashed curve). Both the evolution of the mean ionised fraction and the evolution of the mean neutral fraction obtained from the *rt-sph* simulation have converged.

Schaye J., Dalla Vecchia C., 2008, MNRAS, 383, 1210

Schlittgen R, Streitberg B. H. J., 2001, Zeitreihenanalyse (9. Auflage), Oldenburg Wissenschaftsverlag

Seljak U., Zaldarriaga M., 1996, ApJ, 469, 437

Shapiro P. R., Giroux M. L., Babul A., 1994, ApJ, 427, 25

Sokasian A., Abel T., Hernquist L., Springel V., 2003, MNRAS, 344, 607

　　　Springel V., 2003, MNRAS, 344, 607

Springel V., 2005, MNRAS, 364, 1105

Tegmark M., Silk J., Rees M. J., Blanchard A., Abel T., Palla F., 1997, ApJ, 474, 1

Tegmark M., Zaldarriaga M., 2009, PhRvD, 79, 083530

Valdés M., Ciardi B., Ferrara A., Johnston-Hollitt M., Röttgering H., 2006, MNRAS, 369, L66

Wiersma R. P. C., Schaye J., Smith B. D., 2009, MNRAS, 393, 99

Wise J. H., Abel T., 2005, ApJ, 629, 615

Zahn O., Lidz A., McQuinn M., Dutta S., Hernquist L., Zaldarriaga M., Furlanetto S. R., 2007, ApJ, 654, 12

Zaldarriaga M., Furlanetto S. R., Hernquist L., 2004, ApJ, 608, 622

6.A CHOICE OF RADIATIVE TRANSFER PARAMETERS

In this section we demonstrate that the radiative transfer (RT) simulations that we described in Sec. 6.2.2 employ a sufficiently small RT time step Δt_r and a sufficiently high angular resolution N_c to obtain converged results.

The *rt-sph* simulation employs a time step $\Delta t_r = 10^{-1}$ Myr and an angular resolution $N_c = 32$. We have repeated this simulation at fixed angular resolution $N_c = 32$ using both a larger ($\Delta t_r = 1$ Myr) and a smaller ($\Delta t_r = 10^{-2}$ Myr) time step. In addition, we have repeated this simulation at fixed time step $\Delta t_r = 10^{-1}$ Myr using both a lower ($N_c = 8$) and a higher ($N_c = 128$) angular resolution. Figs. 6.7-6.10 show the results.
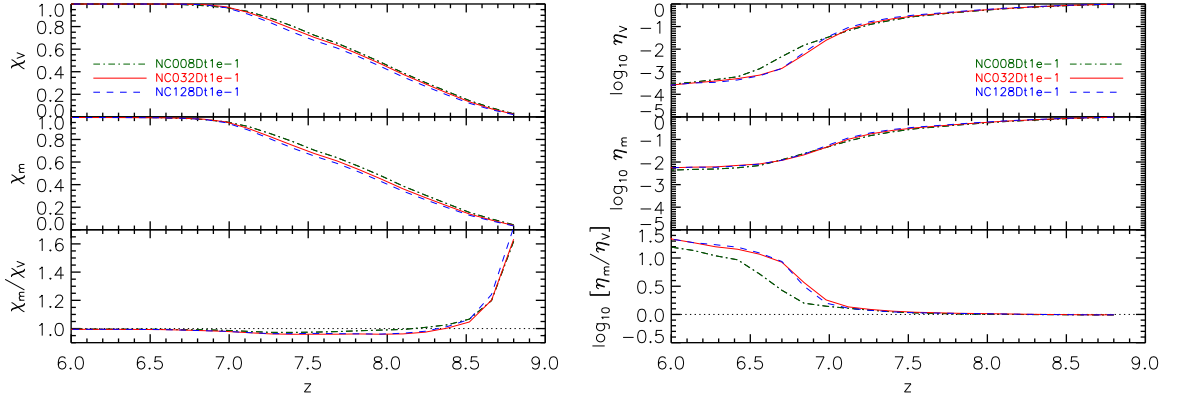
Figure 6.8: Numerical convergence study: angular resolution. The evolution of the the mean ionised (left-hand panel) and the mean neutral (right-hand panel) fraction as obtained in the simulation *rt-sph* (red solid curves), which employed an angular resolution $N_c = 32$ and a time step $\Delta t_r = 10^{-1}$ Myr, is compared to those obtained from identical simulations but using angular resolutions $N_c = 8$ (green dot-dashed curves) and $N_c = 32$ (blue dashed curve). Both the evolution of the mean ionised fraction and the evolution of the mean neutral fraction obtained from the *rt-sph* simulation have converged.
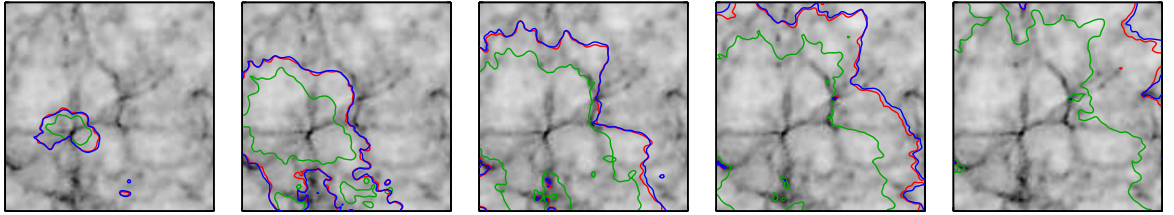
Figure 6.9: Numerical convergence study: RT time step. Slices through the center of the simulation box at redshifts $z = 8.80$, 8.38, 7.96, 7.54, and 7.12 (from left to right). Contours show neutral fractions $\eta = 0.5$ for simulations with fixed angular resolution $N_c = 32$ and radiative transfer time steps $\Delta t_r = 1$ Myr (green), 10^{-1} Myr (red, corresponding to the *rt-sph* simulation) and 10^{-2} Myr (blue). The *rt-sph* simulation has converged with respect to the chosen time step.
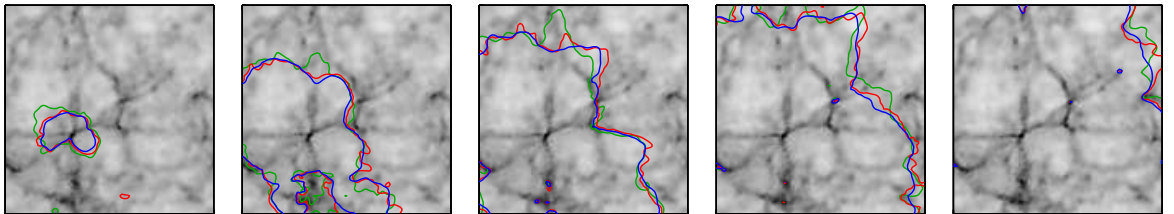
Figure 6.10: Numerical convergence study: angular resolution. Slices through the center of the simulation box at redshifts $z = 8.80$, 8.38, 7.96, 7.54, and 7.12 (from left to right). Contours show neutral fractions $\eta = 0.5$ for simulations with fixed RT time step $\Delta t_r = 10^{-1}$ Myr and angular resolutions $N_c = 8$ (green), $N_c = 32$ (red, corresponding to the *rt-sph* simulation) and $N_c = 128$ (blue). The *rt-sph* simulation has converged with respect to the chosen angular resolution.

Fig. 6.7 shows the evolution of the mean ionised (left-hand panel) and mean neutral (right-hand panel) fractions in the simulations using an angular resolution $N_{\mathrm{c}} = 32$ and time steps $\Delta t_{\mathrm{r}} = 1$ Myr (green dot-dashed curves), $\Delta t_{\mathrm{r}} = 10^{-1}$ Myr (red solid curves) and $\Delta t_{\mathrm{r}} = 10^{-2}$ Myr (blue dashed curves). Note that the red solid curves shown in the left-hand panel of this figure are identical to the red solid curves shown in Fig. 6.2, as they correspond to the same simulation. The results of the simulation with time-step $\Delta t_{\mathrm{r}} = 10^{-1}$ Myr are nearly on top of the results of the simulation with time-step $\Delta t_{\mathrm{r}} = 10^{-2}$ Myr, and hence are converged.

The convergence is confirmed by an inspection of the evolutions of the sizes of the ionised regions that are shown in Fig. 6.9. The figure shows a slice trough the center of the simulation box, generated by mapping the SPH particle densities and neutral fractions to a uniform grid with $\tilde{N}_g = 128$ points per dimension using mass-conserving SPH interpolation. Contours show neutral fractions of $\eta = 0.5$ for the simulations with time steps $\Delta t_{\mathrm{r}} = 1$ Myr (green), $\Delta t_{\mathrm{r}} = 10^{-1}$ Myr (red) and $\Delta t_{\mathrm{r}} = 10^{-2}$ Myr (blue). From left to right, the panels correspond to redshifts $z = 8.8, 8.38, 7.96, 7.54, 7.12$.

The results obtained in the simulation with the largest time step, i.e. with the time step $\Delta t_{\mathrm{r}} = 1$ Myr, are, however, not yet converged. The main reason why the mean ionised fraction and the sizes of the ionised regions predicted by this simulation are systematically smaller than those predicted by the simulations with smaller time steps is that for this simulation our approximate treatment of the time-indepedent RT equation, i.e. the fact that during each RT time step photons are only propagated over a single inter-particle distance (Sec. 5.3.3), becomes inadequate.

Fig. 6.8 shows the evolution of the mean ionised (left-hand panel) and mean neutral (right-hand panel) fractions in the simulations using a fixed time step $\Delta t_{\mathrm{r}} = 10^{-1}$ Myr but varying angular resolutions $N_{\mathrm{c}} = 8$ (green dot-dashed curves), $N_{\mathrm{c}} = 32$ (red solid curves) and $N_{\mathrm{c}} = 128$ (blue dashed curve). The red solid curves shown in the left-hand panel of this figure are identical to the red solid curves shown in Fig. 6.2. Clearly, the results of the simulation with angular resolution $N_{\mathrm{c}} = 32$ are converged, as they are nearly on top of the results of the simulation with the higher angular resolution $N_{\mathrm{c}} = 128$. This is confirmed by a look at the evolution of the sizes of the ionisation fronts shown in Fig. 6.10. The results obtained in the simulation with the lowest angular resolution, i.e. with the angular resolution $N_{\mathrm{c}} = 8$, are, on the other hand, not yet fully converged.

We have not yet discussed the convergence with respect to changes in the time step and the angular resolution for the *rt-grid* simulation. One may expect this simulation to be converged, because it exhibits a smaller dynamic range than the *rt-sph* simulation. We have explicitly verified this expectation by repeating the *rt-grid* simulation with smaller time steps and higher angular resolution (although only for part of the original simulation time).